ACS APPLIED MATERIALS & INTERFACES

www.acsami.org

Research Article

Digital Light Processing 3D Printing of Soft Semicrystalline Acrylates with Localized Shape Memory and Stiffness Control

Adrian K. Rylski, Tejas Maraliga, Yudian Wu, Elizabeth A. Recker, Anthony J. Arrowood, Gabriel E. Sanoja, and Zachariah A. Page*

Cite This: *ACS Appl. Mater. Interfaces* 2023, 15, 34097–34107

Read Online

ACCESS | Metrics & More | Article Recommendations | Supporting Information

ABSTRACT: Multimaterial three-dimensional (3D) printing of objects with spatially tunable thermomechanical properties and shape-memory behavior provides an attractive approach toward programmable "smart" plastics with applications in soft robotics and electronics. To date, digital light processing 3D printing has emerged as one of the fastest manufacturing methods that maintains high precision and resolution. Despite the common utility of semicrystalline polymers in stimuli-responsive materials, few reports exist whereby such polymers have been produced via digital light processing (DLP) 3D printing. Herein, two commodity long-alkyl chain acrylates (C_{18}, stearyl and C_{12}, lauryl) and mixtures therefrom are systematically examined as neat resin components for DLP 3D printing of semicrystalline polymer networks. Tailoring the stearyl/lauryl acrylate ratio results in a wide breadth of thermomechanical properties, including tensile stiffness spanning three orders of magnitude and temperatures from below room temperature (2 °C) to above body temperature (50 °C). This breadth is attributed primarily to changes in the degree of crystallinity. Favorably, the relationship between resin composition and the degree of crystallinity is quadratic, making the thermomechanical properties reproducible and easily programmable. Furthermore, the shape-memory behavior of 3D-printed objects upon thermal cycling is characterized, showing good fatigue resistance and work output. Finally, multimaterial 3D-printed structures with vertical gradation in composition are demonstrated where concomitant localization of thermomechanical properties enables multistage shape-memory and strain-selective behavior. The present platform represents a promising route toward customizable actuators for biomedical applications.

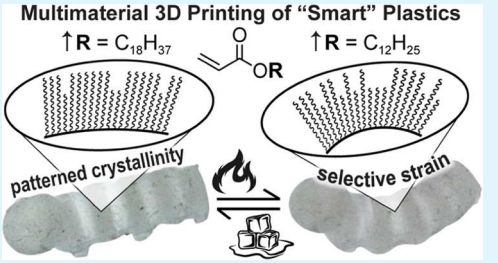

KEYWORDS: *semicrystalline polymer, 3D printing, shape memory, multimaterial, photopolymerization*

Downloaded via UNIV OF TEXAS AT AUSTIN on January 21, 2024 at 15:36:12 (UTC).
See https://pubs.acs.org/sharingguidelines for options on how to legitimately share published articles.

1. INTRODUCTION

Additive manufacturing (three-dimensional (3D) printing) has transformed how society produces plastic objects by enabling the fabrication of geometrically complex shapes with less waste, faster production speeds, and lower equipment cost relative to classical subtractive and molding methods.[1,2] Digital light processing (DLP) 3D printing is one of the fastest forms of vat photopolymerization wherein a liquid resin comprising monomers/crosslinkers and a light-reactive initiator (photoinitiator) is exposed to a series of images from a projector causing localized solidification (photocuring) (Figure 1A). Sequential projections of two-dimensional (2D) images synced with a motorized build platform enable layer-by-layer reconstruction of a 3D object. While great advances have been made with DLP using a wide array of acrylic and epoxy resins, produced parts remain predominantly monolithic and amorphous, resulting in fixed, nonstimuli-responsive thermomechanical behavior (Figure 1B).[3] Refining the resins to enable DLP of multimaterial semicrystalline objects promises to greatly expand the number and diversity of end-use applications by, for example, enabling localization of stiffness and programmable actuation (e.g., shape memory) (Figure 1C). Moreover, 3D-printing stimuli-responsive "smart" objects (a.k.a., "four-dimensional (4D)" printing) has far-reaching utility in biomedical devices, such as wearable health monitors, surgical tools, and implants.[4−8]

Shape-memory phenomena have been demonstrated with many classes of polymers, from hydrogels to thermoplastic elastomers and dynamic thermosets using heat, redox, light, or mechanical force as stimuli to trigger a geometric change.[9] Polymer networks with dynamic, physical cross-links and an easily accessible glass-transition temperature ($T_g \approx 25 \pm 50$ °C) represent the most commonly employed shape-memory materials produced via DLP 3D printing.[10−15] For example, this is highlighted through reversible ionic bonding by Zhao and co-workers,[16] and dynamic urea exchange by Xie and co-workers.[17]

Received: May 19, 2023
Accepted: June 22, 2023
Published: July 7, 2023

ACS Publications

© 2023 American Chemical Society

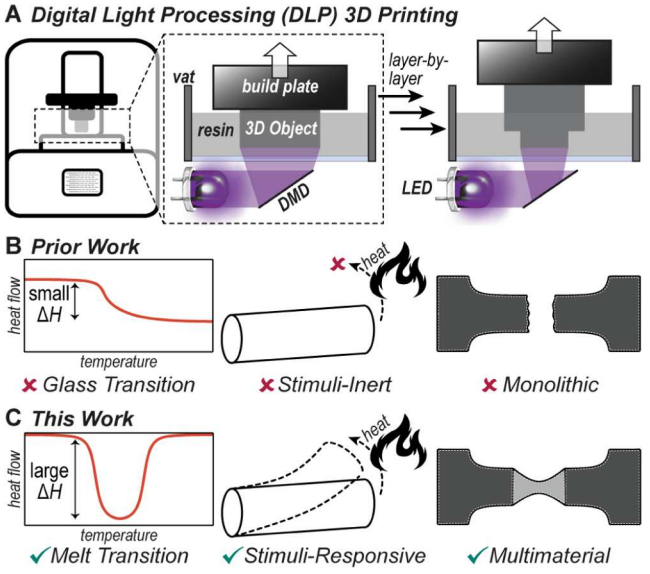

Figure 1. Overview of the process and materials. (A) Schematic of DLP 3D printer highlighting the light source, digital mirror device (DMD) that generates the pattern, vat with liquid resin, and additive nature of the process. (B) Prior work with DLP most commonly produces materials that are amorphous, nonresponsive to stimuli, and compositionally uniform (monolithic). (C) This work systematically examines DLP 3D printing of semicrystalline, thermally responsive, multimaterial objects.

Another strategy of obtaining shape memory that has been less commonly implemented in DLP 3D printing is through controlling molecular order of polymer chains rather than chemical cross-linking between them. For example, (meso)-phase transitions between crystalline and isotropic (amorphous) states upon heating/cooling have been used extensively for shape-memory applications with 2D liquid crystalline and semicrystalline polymers.[18−21] In contrast to T_g, a kinetic phenomenon, the melting temperature (T_m) is associated with a first-order phase transition that results in a sharp, energic change in morphology, exemplified by the large enthalpy of melting ($\Delta H_m \approx 10-100$ J/g).[22,23] Thus, actuation through T_m can be both rapid and result in a large/reversible deformation with a high output of latent energy that can translate into work. However, only a few examples of semicrystalline shape-memory polymers prepared by vat photopolymerization 3D printing exist.[24−31] One such approach by Ge and co-workers involves adding semicrystalline poly(caprolactone) into a methacrylic resin, where it was demonstrated that between 10 and 50% poly(caprolactone) provided stiff plastics (tensile moduli, E > 50 MPa) with melting enthalpies ranging from ∼7 to 32 J/g, and shape recovery ratios of 83−95%.[27,28] Another example by Furukawa and co-workers describes the incorporation of acrylic monomers containing long, saturated n-alkyl chains into acrylamide-based resins to prepare shape-memory hydrogels, where the monomer ratios were varied to tune the degree of semicrystallinity, water equilibrium swelling between ∼60 and 10% and elastic modulus E between 0.5 and 26.9 MPa.[29] Despite these promising examples, DLP 3D printing of neat semicrystalline resins to access shape-memory materials has yet to be thoroughly examined, with no known cases of multimaterial printing where properties are localized in predefined space (e.g., layers).

Accessing multimaterials with spatial control over disparate thermomechanical properties, such as T_m and stiffness, represents an ongoing challenge in the field of 3D printing.[32−34] An additional challenge when considering biomedical applications is manufacturing soft materials with tissue-mimetic moduli (<1 MPa) to preclude activation of chronic inflammatory responses.[35,36] To these points, major hurdles include premature mechanical failure because of weak interfacial adhesion[37−40] and large tensile moduli ≥1 MPa due to physical entanglements.[41,42] State-of-the-art methods for multimaterial DLP 3D printing that can provide good interfacial adhesion via covalent bonding between the various applied chemistries include modifications of the resin/resin vats, multiwavelength, and grayscale printing.[33,43−48] Of these, the addition of monomer to the vat during the course of printing provides a straightforward and broadly accessible method. Albeit limited by heterogeneities along the build direction (z-axis), this method allows for the examination of (gradient) interfaces as the composition is changed from layer to layer, which is of paramount importance in multimaterial structures.

Recently, we demonstrated that thermomechanical properties, such as stiffness and crystallinity, could be spatially tailored in 2D (films) by controlling main-chain packing via a dual catalysis strategy.[49] As an alternative, side-chain crystallization from monomers bearing long n-alkyl groups was envisioned as an avenue toward spatially tailoring thermomechanical properties, while also reducing entanglement density to decrease stiffness in analogy to pressure-sensitive adhesives[50] and bottlebrush polymers with impressively low moduli ranging from ∼0.1 to 500 kPa.[51,52] Herein, this is accomplished via DLP 3D printing using resins composed primarily of commodity long-alkyl chain acrylates, namely, stearyl acrylate (SA) and lauryl acrylate (LA). The ratio of SA/LA provides a handle to tailor semicrystallinity and in-turn the thermomechanical properties and stimuli-responsive shape-memory behavior (Figure 1C). Furthermore, it provides a direct avenue toward multimaterial objects with vertical property gradients. The resultant 3D objects have potential utility as soft actuators for biomedical applications.

2. RESULTS AND DISCUSSION

2.1. Resin Formulation and Photocuring. The initially selected resin formulation was a simple mixture of SA and/or LA, along with tripropylene glycol diacrylate (1 wt %) for light cross-linking and bisacylphosphine oxide (BAPO, 1 wt %) as a traditional Norrish type I photoinitiator (Figure 2A). Notably, SA has a melting temperature of 28 °C and is thus solid at room temperature. This prompted us to first screen mixtures of SA and LA that were liquid at room temperature, finding a qualitative upper threshold of around 75 wt % SA, 25 wt % LA (i.e., not including cross-linker and photoinitiator). The polymerization kinetics under printing-relevant conditions (405 nm light-emitting diode (LED), 10 mW/cm^2 intensity) were determined next using real-time Fourier transform infrared (RT-FTIR) spectroscopy at both room temperature (23 °C) and 40 °C, monitoring the C═C overtone stretch at 6100 cm^{-1} (Figures 2B and S3). At room temperature, it was noted that increasing SA content from 0 to 75 wt % SA resulted in a slight decrease in rate from 0.46 to 0.42 M/s, which was attributed to a decrease in the concentration of acrylate moieties. However, in terms of rate (%/s) and time to maximum acrylate consumption all three conditions were

https://doi.org/10.1021/acsami.3c07172
ACS Appl. Mater. Interfaces 2023, 15, 34097−34107

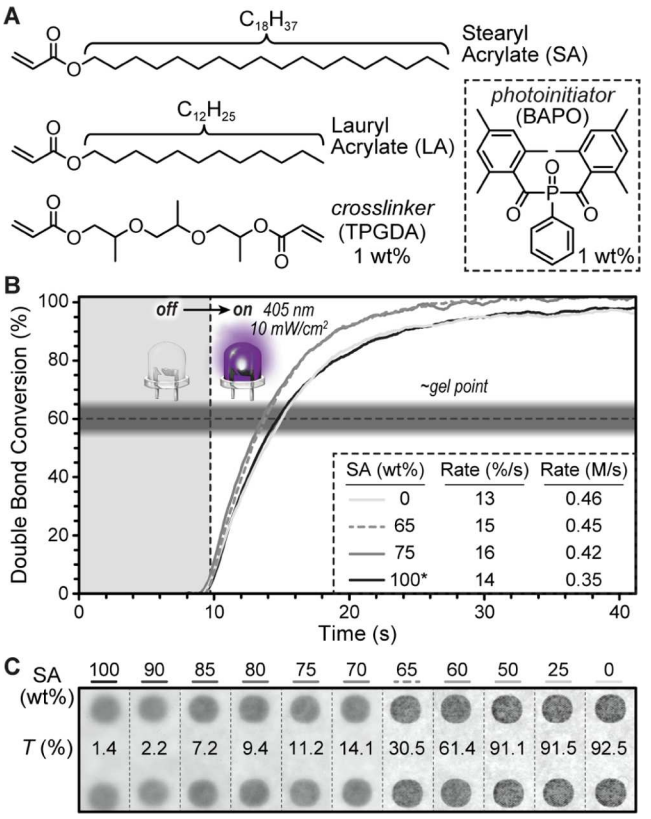

Figure 2. Resin formulation and photocuring. (A) Chemical composition for acrylate monomers, cross-linker, and photoinitiator. BAPO = bisacylphosphine oxide. (B) Real-time Fourier transform infrared spectroscopy to monitor monomer conversion during irradiation with 405 nm light. Polymerization rate provided in the inset. *Measured at 40 °C. Shaded line represents a rough estimate of conversion at the gel point, determined using photorheology. (C) Photograph of resulting films sitting atop a piece of dotted paper. Values for the percent visible transmittance (400−700 nm) are provided.

similar (13−16 %/s, >90% C═C conversion). To enable characterization of formulations having >75 wt % SA (solids at room temperature), a custom near-infrared (near-IR) transparent indium tin oxide (ITO)-coated glass heater was constructed, which contained a thermocouple to precisely control temperature during RT-FTIR measurements (see the Supporting Information for details). Monitoring the photopolymerization at 40 °C showed no significant difference in the kinetics, which agrees with prior reports on temperature effects for photoinitiated acrylate polymerizations.[53] Next, photorheology under identical conditions (405 nm LED, 10 mW/cm^2 intensity) was performed to determine the time to gelation, identified as the crossover of storage and loss moduli ($\tan\delta = 1$),[54] which serves as an approximation for the minimum exposure time required in layer-by-layer 3D printing (Figures 2B and S4). In all cases, gel points were observed between ∼3.4 and 4.4 s after irradiation began. This timing corresponds to a conversion of roughly 60%, which is attributed to a low cross-link density that arises from a small tripropylene glycol diacrylate (TPGDA) loading and long side chains that limit entanglements.

From these reactivity experiments, the cured films had a notable difference in opacity where increasing SA content resulted in decreased transmittance of visible light (Figure 2C). Spectrophotometry was performed to quantify the percent visible light transmittance (400−700 nm), providing a range from 1.4 ± 0.1 to 92.5 ± 0.3% for 100 to 0 wt % SA, respectively (Figure S5). The change in opacity was hypothesized to arise from a difference in crystallinity, which prompted thermal characterization.

2.2. Thermomechanical Characterization. With the aim of obtaining the widest breadth of thermomechanical properties, two variables were initially examined using differential scanning calorimetry (DSC) and uniaxial tensile testing to failure. Specifically, the following variables were studied: (1) SA/LA ratio at a constant TPGDA content (1 wt %) and (2) TPGDA wt % at a constant SA/LA ratio of 75:25 (75 wt % SA). During this screening, it was found that varying the SA/LA ratio resulted in larger variations in thermomechanical properties (Figures S6−S8). Subsequent investigations emphasized a systematic change in the SA/LA ratio.

To this regard, ΔH_m and T_m were characterized for photocured samples using DSC (Figure 3A). A clear trend

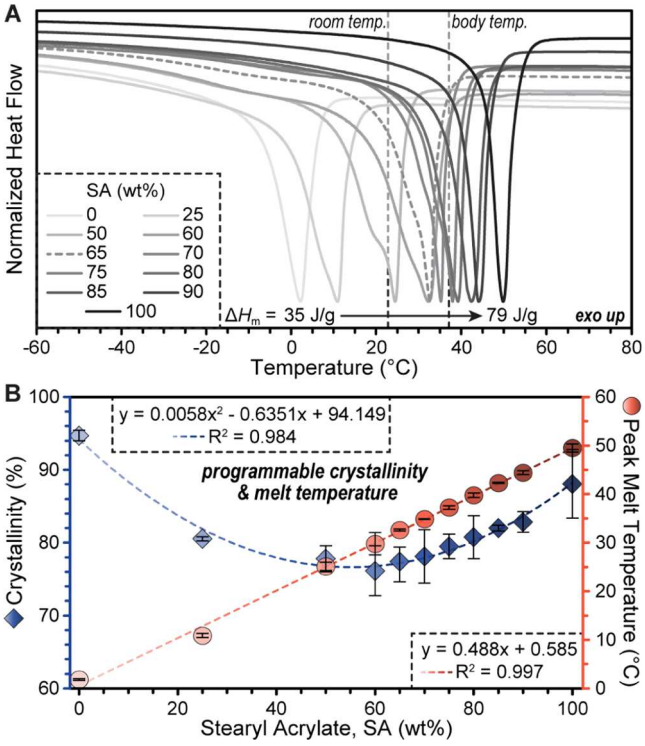

Figure 3. Thermal characterization. (A) Differential scanning calorimetry showing clear melt transitions with the range in melt enthalpy values provided. (B) Relationships between stearyl acrylate (SA) content and the percent crystallinity and peak melt temperature. Dashed lines represent fits to the data, with corresponding equations provided as insets. Symbols represent an average of 3 measurements with error bars being ± 1 standard deviation from the mean.

emerged with ΔH_m increasing from 35.4 ± 0.2 to 78.6 ± 4.2 J/g in going from 0 to 100 wt % SA. From these measurements, the degree of crystallinity (χ_c) can be estimated using the following formula eq 1, provided ΔH_m values for "100%" crystalline LA and SA polymers—36.6 and 89.3 J/g, respectively[55]

$$\chi_c = \frac{\Delta H_m}{([SA] \times \Delta H_{SA,\,100\%}) + ([LA] \times \Delta H_{LA,100\%})} \quad (1)$$

https://doi.org/10.1021/acsami.3c07172
ACS Appl. Mater. Interfaces 2023, 15, 34097−34107

where [SA] and [LA] are the weight fraction of each, respectively (Figure 3B). This analysis revealed that χ_c could be tuned between ~76 and 94% in a predictable manner that empirically follows a second-order polynomial (quadratic) relationship. Additionally, peak T_m values increased in a controllable linear manner from 1.7 ± 0.2 to 49.5 ± 0.8 °C in going from 0 to 100 wt % SA (Figures 3B and S9). Notably, body temperature (~37 °C) is within this range, making it of biological relevance. Finally, thermal decomposition temperatures for 0 and 100 wt % SA were measured using thermogravimetric analysis, finding a 5% weight-loss temperature (T_{d5}) of 237 and 238 °C, respectively (Figure S10). The influence of resin formulation (SA/LA ratio) on the bulk mechanical properties (i.e., stress−strain response) was examined next. Horizontal tensile specimens (dogbones) of the ASTM-D638 type IV scaled by 0.3× were rapidly produced via DLP 3D printing (405 nm, 10 mW/cm^2, 4 s/layer). Uniaxial tensile testing was then performed until failure on a minimum of 5 specimens per formulation (Figures 4A, S11, and S12). The E (tensile moduli) at room temperature (23 °C) were highly dependent on SA content, with values spanning three orders of magnitude from 180 ± 54 to 0.08 ± 0.01 MPa for 100 and 0 wt % SA, respectively. An iterative cycle loading-and-unloading test where strain is increased in a stepwise fashion (Strobl analysis) was performed on the 60−65 wt % SA specimens at room temperature, which showed considerable hysteresis and plastic deformation (Figures S13−S15).[56] However, shape recovery was observed upon heating, consistent with behavior previously reported for semicrystalline polymers.[18−21] The influence of exposure time and print angle on mechanical properties was also examined, revealing embrittlement upon increasing from 4 to 10 s/layer and negligible anisotropy associated with print orientation (Figures S16 and S17). Thus, with this method, rigid plastics (E > 50 MPa) and supersoft elastomers (E < 100 kPa) could be obtained simply by toggling the SA/LA ratio in the resin.

The mechanical properties obtained from uniaxial tensile testing were then coupled with the melting temperatures obtained from DSC to gain insight into their relationship and inform formulation selection for further experimentation (Figure 4B,C). Relating modulus to the melt onset temperature showed a direct relationship. Samples comprised of <60 wt % SA were very soft and qualitatively adhesive, making them more difficult to handle (Figure 4B red shaded region) relative to samples with 60−70 wt % SA (Figure 4B green shaded region). In these latter samples, it was postulated that the degree of crystallinity existing at room temperature makes them more processable, yet they remain fairly soft (E < 50 MPa). Going to contents >70 wt % SA results in a direct linear relationship between E and melt onset temperature (Figure 4B blue shaded region). However, in comparing E to strain at fracture (ε_f), a clear gap exists for this system in going from 75 to 80 wt % SA, where samples become much more brittle with ε_f values dropping from ~100 to <10% (Figure 4C green to blue shaded regions). Additionally, samples with a SA wt % between 60 and 75 had >100× higher strain energy density (U), suggesting that this range provides an ideal balance of soft and semicrystalline (stiff) phases to mitigate nucleation and propagation of cracks by plastic deformation (Figures 4C and S11). Based on these results, the degree of crystallinity at room temperature was hypothesized to govern the measured thermomechanical behaviors. Overall, the system is highly tunable in its thermomechanical properties, and clear relationships enable the user to dial in a particular property of interest. Herein, further experimentation largely focused on the 60−75 wt % SA formulations given the large disparity in mechanical properties (E of ~8−60 MPa and ε_f of ~100−260%) and optimal combination of stiffness and toughness that occur with small changes in composition while also enabling room-temperature printability.

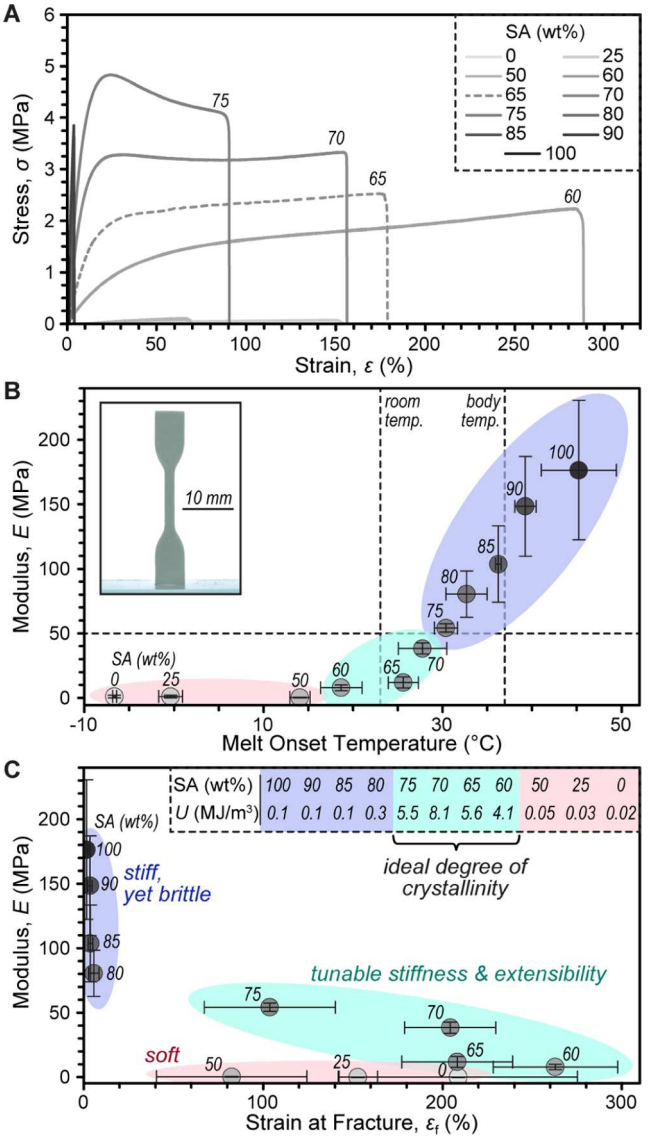

Figure 4. Mechanical characterization. (A) Stress−strain plot showing the effect of stearyl acrylate (SA) content on bulk mechanical properties under uniaxial tension. (B) Relationship between modulus and melt onset temperature with dashed line at E = 50 MPa. Inset: photograph of representative dogbone (75 wt % SA) used for tensile testing. (C) Relationship between modulus and strain at fracture. Symbols represent an average of 5 or more measurements with error bars being ± 1 standard deviation from the mean. Inset provides strain energy density (U).

2.3. Shape-Memory Characterization. After identifying composition−thermomechanical relationships, shape-memory behavior for the 75 wt % SA materials (ΔH_m = 61 ± 1 J/g) was examined. An initial qualitative analysis was performed with a complex lattice structure (Kelvin foam) containing features as small as ~400 μm, demonstrating the good resolution and fidelity of the current DLP 3D-printing process (Figure S18).

https://doi.org/10.1021/acsami.3c07172
ACS Appl. Mater. Interfaces 2023, 15, 34097−34107

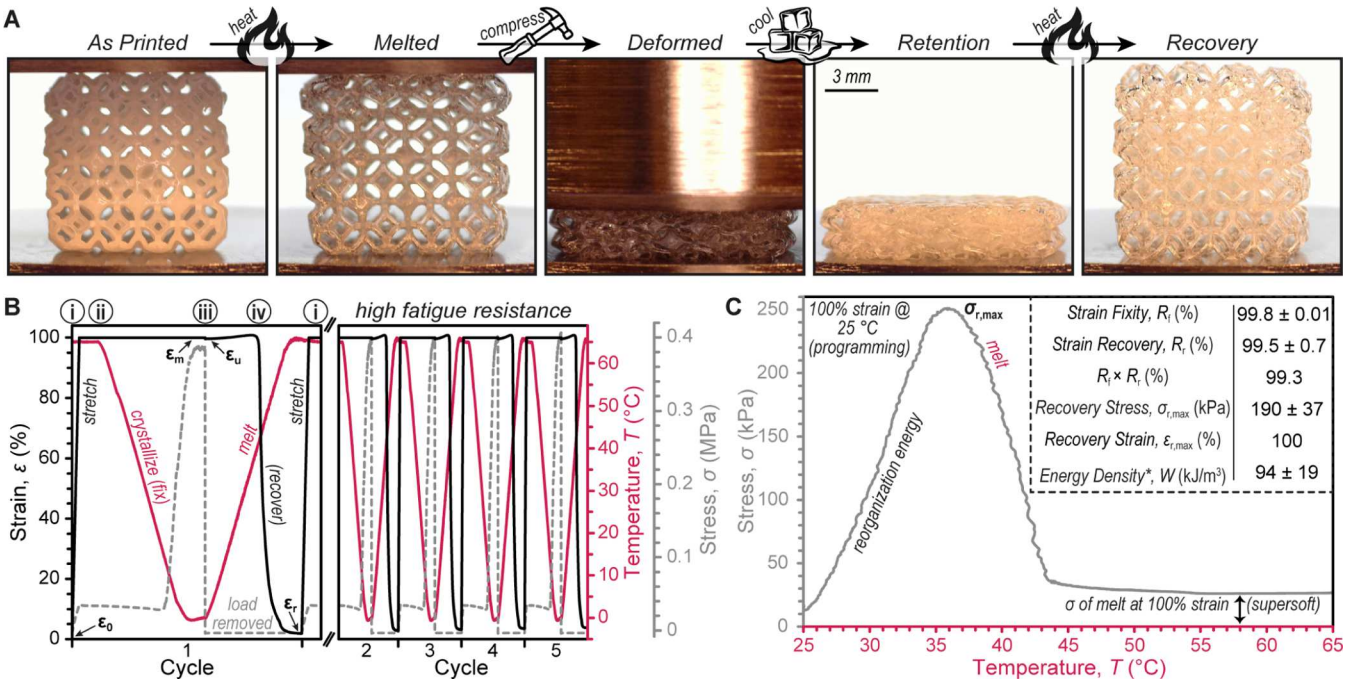

Figure 5. Shape-memory characterization. (A) Images of 3D-printed Kelvin foam (75 wt % SA) undergoing sequential shape programming and recovery with 75% compression of the original shape. (B) Shape-memory behavior of a 75 wt % SA sample undergoing cyclic unconstrained shape recovery. ε_0 = initial strain, ε_m = max strain, ε_u = strain after unloading, and εr = strain after recovery. (C) Representative shape recovery of the champion (max stress) 75 wt % SA sample fixed at 100% strain, providing insight into key shape-memory parameters. *Estimated energy density (details in the Supporting Information).

The ability to retain this lattice structure ("permanent shape") was then exhibited in a multistep sequence (Figure 5A and Movie S1). First, the object was heated past its T_m (>40 °C), followed by compressing it to 25% its original height (i.e., 75% strain). Next, the object was allowed to cool to room temperature to fix it in the compressed state upon removing the load ("temporary shape"). Finally, heating the sample above T_m resulted in a rapid recovery of the original lattice shape.

To quantify the shape-memory behavior, thermal cyclic recovery testing was performed using dynamic mechanical analysis on DLP 3D-printed samples comprised of 75 wt % SA (Figure 5B). Each sample had an ASTM-D638 type IV dogbone geometry (scaled by 0.3×) and was measured under uniaxial tension. Unconstrained recovery tests, wherein the stress or strain is controlled and monitored at different stages of heating and cooling, were performed to determine the shape-memory fixity ratio (R_f) from maximum strain (ε_m) and strain after unloading (ε_u) (eq 3, Section 4) and the shape-memory recovery ratio (R_r) from the initial strain (ε_0) and strain after recovery (ε_r) (eq 4, Section 4). These values provide a quantitative measure of a sample's ability to maintain the temporary (fixed) shape and to return to the permanent (original) shape, respectively. In a typical experiment, a sample with thermal history erased was clamped, heated to 65 °C (melted), and then stretched to 100% strain (2× its original length, initial stretch rate 200%/min) while monitoring stress (Figure 5B, stage (i)). The sample stress increased to 37 kPa and showed little-to-no stress relaxation upon holding at 100% strain and 65 °C for a few minutes. Maintaining a fixed strain of 100%, the sample was cooled to 0 °C, which led to crystallization and a corresponding increase in stress to ∼390 kPa (Figure 5B, stage (ii)). At this point, the sample was "fixed" in a temporary shape, and the measurement was switched from strain control to load control, setting stress to ∼0, which resulted in a 0.4% drop in strain that corresponds to the strain fixity (Figure 5B, stage (iii)). Heating the sample led to a slight expansion before melting at around 40 °C. Upon melting, the sample rapidly recovered to the permanent shape, as noted by a decrease in strain to ∼3% (Figure 5B, stage (iv)). This process was repeated an additional four times, showing excellent reversibility. From this cycling, an average R_f of 99.8 ± <0.01 and R_r of 99.5 ± 0.7 were calculated (see the Supporting Information for details), indicating that this material provides idealized shape-memory behavior (Figure 5C, inset).

To estimate the strain energy density (W) of 75 wt % SA, a measure of work output, a series of constrained shape recovery experiments were performed, again using dynamic mechanical analysis on DLP 3D-printed samples in ASTM-D638 type IV geometry (scaled by 0.3×) under uniaxial tension. First, samples were annealed at 80 °C, cooled to room temperature, clamped, and cycled from 25 to 65 °C to ensure thermal history was erased. Samples were then deformed to 100% strain ($\varepsilon_{r,max}$) while being held at a temperature of 25 °C, placing them in a semicrystalline state. Samples were held at this strain undisturbed for ∼10 min, followed by heating to 65 °C at 3 °C/min, while measuring stress (Figure 5C). An increase in stress before the peak melt temperature (37 °C) is hypothesized to arise from crystal growth and/or a reorganization energy as melting begins while the stiffness of the sample is high relative to that from a fully amorphous state.[9] The stress peaked around the peak melting temperature, providing a maximum recovery stress ($\sigma_{r,max}$) value of 190 ± 37 kPa. From this value, W was calculated to be 94 ± 19 kJ/m^3 using the following equation

https://doi.org/10.1021/acsami.3c07172
ACS Appl. Mater. Interfaces 2023, 15, 34097−34107

$$W = \frac{(\sigma_{r,max}) \times (\varepsilon_{r,max})}{2} \quad (2)$$

that assumes a linear relationship between the constrained and unconstrained recovery, as described previously in the literature.[57,58] A W of ∼100 kJ/m^3 is within the same order of magnitude as compared to previously reported low modulus (≤50 MPa) shape-memory materials.[59−65] Additionally, the stress remaining in the sample once melted (∼30 kPa) is comparable to that observed for a sample deformed to 100% strain starting at 65 °C (Figure S19), again demonstrating excellent recovery behavior while displaying supersoft (<100 kPa) mechanical properties.

2.4. Multimaterial Printing and Characterization. To spatially tailor thermomechanical properties, multimaterial 3D printing was accomplished by controlling the SA/LA ratio along the build (z) direction through addition of monomer to the vat mid-print (Figure 6A). Accurate and precise control of resin composition during multimaterial 3D printing was achieved by estimating the change in resin volume from each layer via the digital input and characterizing resin density to determine how much SA or LA containing 1 wt % BAPO and TPDGDA to add (Figure S20).

This multimaterial 3D-printing method was first applied to create rectangular bars with three sections comprised of 90, 75, and 60 wt % SA by adding LA-based resin at two distinct points during the print (Figure 6B). The multishape recovery behavior of the printed object was then demonstrated by first heating the sample, physically twisting it, and then cooling it back to provide the temporary (twisted) shape. The sample was then glued at one end, placed in a temperature-controlled chamber, and heated at a rate of 2 °C/min while recording (Movie S2). Still images from the video show the distinct points of recovery for each segment, which occurred in accord with the melt temperatures for the particular SA/LA compositions (Figure 6B). This experiment showcased how subtle changes in local composition can be leveraged to achieve sequential shapeshifting and harness multistimuli-responsive materials that are sensitive to small environmental changes, such as temperature.[66]

To assess the strength of the interfacial gradient and demonstrate selective straining, multimaterial samples for tensile testing were prepared (ASTM-D638 type IV scaled by 0.3×). These samples were printed vertically where the top and bottom quadrants of the gauge were composed of 75 wt % SA (stiff domains), and the middle half of the gauge was composed of 65 wt % SA (soft domain) (Figure 6C inset). Selective straining at room temperature (∼23 °C) of the softer middle section was then quantified using digital image correlation. Upon stretching the sample under uniaxial tension until failure, the soft domain experienced >150% strain, while the stiff domains experienced <4% strain, which agreed with the theoretical strain values for these formulations (Figure 6C). This is consistent with a spring-like model of the domains in series, thus both experiencing the same stress, which predicts a theoretical strain value of ∼5% for the stiff domains when the global strain is ∼70%, coincident with failure of the soft domain (see the Supporting Information for details). This experiment showcased how small changes to SA/LA ratio mid-print can be utilized to access multimaterial objects with locally disparate mechanical properties, which has potential utility in wearable electronics technology.

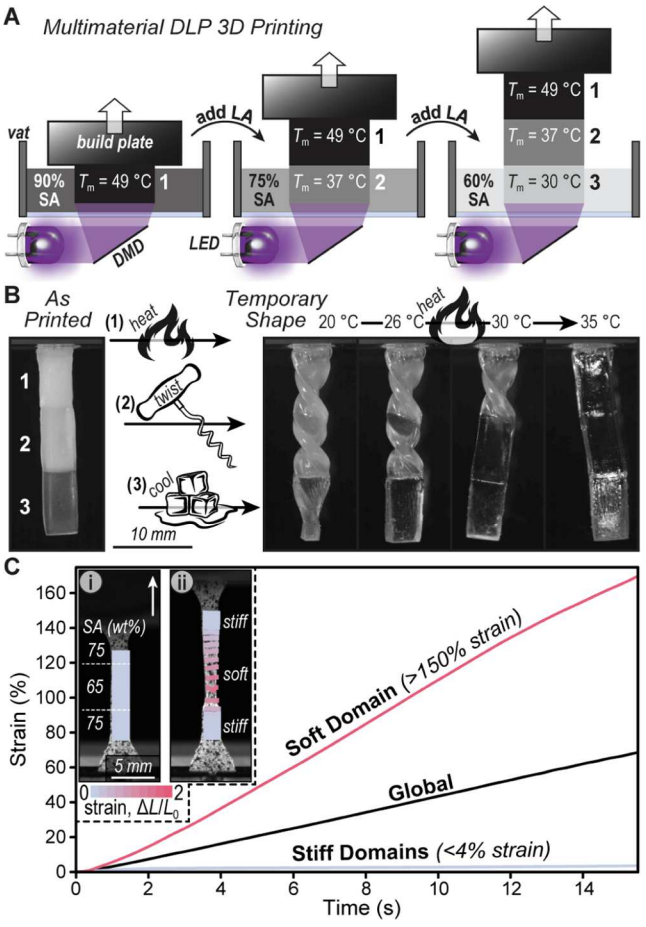

Figure 6. Multimaterial 3D prints. (A) Illustration of sequential LA addition mid-print to achieve multimaterial 3D objects. (B) Images of multimaterial bar containing 90, 75, and 60 wt % SA, showing multistage shape-memory (recovery) behavior upon controlled heating. (C) Digital image correlation of multimaterial tensile specimen containing top and bottom quadrants composed of 75 wt % SA and a middle segment of 65 wt % SA, demonstrating selective straining behavior.

3. CONCLUDING REMARKS

Herein, a comprehensive multimaterial 3D-printing strategy was developed that leverages tunable side-chain crystallization from readily available acrylate monomers as a means to spatially control properties. By varying the ratio of lauryl (C_{12}) and stearyl (C_{18}) acrylate monomers in a photocurable resin, 3D-printed polymeric objects with a wide range of thermomechanical properties were achieved, including peak melt temperatures from 2 to 50 °C, degree of crystallinity from 76 to 94%, enthalpy of melting from 35 to 79 J/g, moduli from 0.08 to 180 MPa, strain at break from 2 to 260%, and strain energy density from 0.1 to 8.1 MJ/m^3. The softness of these materials in the melt arises from their long side chains, providing a "brush-like" architecture that reduces entanglements, which, taken together with melt transitions that occur near body temperature, makes them particularly relevant for biomedical applications. Furthermore, 3D-printed structures were shown to have excellent shape-memory properties, with near unity recovery and fixity. Additionally, energy densities near 100 kJ/m^3 were achieved, which is competitive with state-of-the-art shape-memory materials also displaying low moduli

https://doi.org/10.1021/acsami.3c07172
ACS Appl. Mater. Interfaces 2023, 15, 34097−34107

(≤50 MPa). Finally, spatial localization of different SA/LA compositions enabled the production of multimaterial objects with unique metamaterial behaviors, including multistage, programmable shape memory and strain selectivity. Insight from this work is anticipated to guide advancements in multimaterial manufacturing that leverage local changes to crystallization. From an application perspective, such structures have practical utility in soft actuators and wearable electronics for biomedical purposes.

4. EXPERIMENTAL SECTION

4.1. Materials. All chemicals were used as received. Stearyl acrylate (SA) (>97%), lauryl acrylate (LA) (>98%), and tripropylene glycol diacrylate (TPGDA) (>90%) were purchased from TCI. Phenylbis(2,4,6-trimethylbenzoyl) phosphine oxide (BAPO) (97%) was purchased from Sigma-Aldrich.

4.2. Sample Preparation. To a 40 mL scintillation vial was added 25 g of monomer (SA or LA). The SA monomer was melted before addition using either an oven or a heat gun. To this was added 250 mg (1.00 wt %) of TPGDA and 250 mg (1.00 wt %) of BAPO. This resin mixture was then sonicated in warm water for 30 min or until no visible precipitate remained. If the SA formulation began to solidify due to the water temperature being below the melting point of SA, the vial was removed and melted with a heat gun before returning it to the sonication bath. When the resin formulation (SA/LA) was modified, the necessary amount of SA and LA resin, as prepared above, was added to a new scintillation vial that was vortex mixed and heated by a heat gun if necessary. When testing the influence of the cross-linker, the resin was prepared by preparing a formulation of 75 wt % SA and 25 wt % LA with 1% BAPO present. To this resin was added the necessary amount of TPGDA to reach the desired cross-link content.

4.3. Real-Time Fourier Transform Infrared Spectroscopy (RT-FTIR). Resin formulations were introduced between two 1 mm thick glass microscope slides (cat. no. 12-550-A3, Fisher Scientific) separated by ∼100 μm polyester plastic shims (cat. no. 9513K66, McMaster-Carr) to maintain a constant sample thickness over the course of the photopolymerization. Each sample was placed in a horizontal transmission accessory (A043-N/Q, Bruker) equipped on the FTIR spectrometer (INVENIO-R, Bruker), which was controlled using OPUS spectroscopy software. Spectra were collected from 2000 to 7000 cm^{-1} at a rate of 1 scan every 0.36 s. Only samples that were liquid at room temperature (∼25 °C) were monitored at STP conditions. All samples were additionally monitored at an elevated temperature of 40 °C by heating the resin on a hot plate to 40 °C and then using a heated stage that maintained a constant temperature of 40 °C during the entirety of the experiment. Heated RT-FTIR was performed using a custom-built heating stage comprised of a 50 mm × 50 mm × 0.7 mm section of indium tin oxide-coated glass with a resistance of ∼10 Ω (MXBAOHENGus Instrument Co.) (Figure S1). The stage was heated using a 12 V DC power supply via electrodes attached to the lateral edges of the stage with conductive copper tape. Temperature control was achieved using an Inkbird ITC-100VH PID temperature controller and an Inkbird 12 V DC solid state relay. The temperature of the stage was evaluated using a K-type thermocouple (Smartsails) located on the anterior edge of the heated stage. These heated FTIR experiments also allocated a short waiting period of about 20 s to allow for temperature equilibration between the heated plate, glass slide, and resin before starting the experiments. The functional group conversion was determined by monitoring the disappearance of the peak area centered at ∼3100 cm^{-1} corresponding to the C═C stretch and ∼6100 cm^{-1} for the overtone. A liquid light guide was used to illuminate the samples using a 405 nm LED connected to a driver from which light intensity could be controlled remotely through software (Mightex). Each sample was tested in triplicate at an intensity of 10 mW/cm^2.

4.4. Photorheology. Photorheology experiments were completed using a Discovery HR 20 hybrid rheometer from TA Instruments (TA Instruments, DE). The rheometer was equipped with a "UV light guide" accessory, a 20 mm diameter acrylic bottom plate, and a 20 mm diameter geometry aluminum upper parallel plate. Additionally, an upper heated plate was used for experiments performed at an elevated temperature of 40 °C. A liquid light guide was used to illuminate the samples using a 405 nm LED connected to a driver from which light intensity could be controlled remotely through software (Mightex). Each sample was tested in triplicate at an intensity of 10 and/or 15 mW/cm^2.

4.5. UV−vis Transmittance Measurements. UV−vis transmission spectroscopy was performed with polymer films (∼250 μm thick) encased in glass slides on a horizontal transmission accessory (Stage RTL-T, Ocean Optics) connected to a spectrometer (QE PRO-ABS, Ocean Optics) through optical fibers. The spectrometer measured in the range from 200 to 950 nm, at an optical resolution of 1.7 nm, using a back-thinned, TE cooled, 1024 × 58 element CCD array. A deuterium−tungsten halogen light source (DH-2000-BAL) was used as the probe light. Tuned for absorption measurements, this system utilized a balanced deuterium−tungsten halogen light source (DH-2000-BAL) with a typical output of 194 μW (deuterium bulb) and 615 μW (tungsten bulb) through an SMA 905 connector, covering a range from 230 nm to 2.5 μm. Multimode fiber-optic cables with SMA connectors on both ends and a 600 μm core diameter (QP600-025-SR) connected the light source to the sample holder. Transmittance measurements were performed in triplicate using the Ocean Optics software.

4.6. 3D Printing. 3D printing was performed using a custom, digital light processing (DLP) 3D printer (Monoprinter, MA) (Figure S1). The printer was equipped with a violet LED (Luminus CBT-120-UV) that has a full width at half-maximum (FWHM) of 16 nm. The light intensity measured at the resin vat floor was ∼10.0 mW/cm^2, which was used for all prints in this study. Custom software (MonoWare) was used to import STL design files and digitally slice them into a sequence of 2D image files for projection. The projector resolution was 1920 × 1080 pixels, with each pixel being 20 μm × 20 μm at the image plane. The maximum build plane for the printer in its current configuration is 38.4 mm × 21.6 mm, and a vat with the dimensions of 56 mm × 35 mm × 25 mm (length × width × height) was used. A transparent fluorinated polymer film (NFEP film, Siraya Tech) was used as the base of the resin tank to provide a nonstick and flexible surface. The predetermined layer thickness for each slice of the 3D print was 50 μm, with an exposure time of 8 s for the first 2 layers and 4 s for all subsequent layers, unless otherwise stated. An opaque acrylic chamber was placed over top of the printing area to minimize exposure from external light sources for all resins containing 75% SA or less, as the resin remained free-flowing. For resin containing 80% SA or more, a custom opaque acrylic heating chamber developed by Monoprinter (1CH Temp. Cont.) was used and set to 40 °C to ensure that the resin would remain liquid during the printing time (Figure S2). After completion of the 3D print, the printed object was rinsed with acetone and postcured for 5 min using a Wash & Cure Machine 2.0 (Anycubic) with a maximum emission wavelength at 405 nm and an average intensity of 0.9 mW/cm^2.

4.7. Differential Scanning Calorimetry (DSC). DSC was performed using a TA Instruments DSC2500 with a heat−cool−heat method ramping at 10.00 °C/min with a range starting at −90 °C and ending at 100 °C. Data was collected from the printed specimen and performed in triplicate on three different samples to obtain average and standard deviation.

4.8. Thermogravimetric Analysis (TGA). TGA was performed on a TA Instruments TGA Q500 with a heat ramp set at 5.00 °C/min with a range starting at 25 °C and ending at 800 °C.

4.9. Uniaxial Tensile Testing. Tensile testing was carried out using a Shimadzu Autograph AGS-X universal testing machine equipped with a 10 kN load cell. Samples were printed as an ASTM Standard D638 Type IV scaled by a factor of 0.3 (∼2.2 mm width, 10 mm gauge length, 1.3 mm thickness). Axial extension was carried out at 20 mm/min (200%/min) until fracture.

4.10. Strobl Analysis. Step cycle tensile testing was carried out using a Shimadzu Autograph AGS-X universal testing machine equipped with a 10 kN load cell. Samples were printed as an ASTM

https://doi.org/10.1021/acsami.3c07172
ACS Appl. Mater. Interfaces 2023, 15, 34097−34107

Standard D638 Type IV scaled by a factor of 0.3 (~2.2 mm width, 10 mm gauge length, 1.3 mm thickness). Axial extension was carried out at 20 mm/min (200%/min) until fracture. Elastic recovery and plastic deformation were extrapolated from straining 5, 10, 20, 30, 40, 50, 75, 100, 125, 150, 175, 200, 250, and 300%.[67]

4.11. Dynamic Mechanical Analysis (DMA). DMA experiments were carried out using a TA DMA 850 which can be equipped with tension, three-point bending, or compression clamp. With different clamps, it can provide various kinds of mechanical property tests to materials. The motor of DMA 850 can deliver continuous forces from 0.1 mN to 18 N with a force resolution of 0.01 mN and a strain resolution of 0.1 nm. When sinusoidal stress is applied, the frequency can be controlled between 0.001 and 200 Hz. The furnace of the DMA 850 can heat up the material to 600 °C, and with liquid nitrogen attached, the material can be cooled to −160 °C. The software of the instrument is TRIOS from TA instrument.

4.11.1. DMA Temperature Sweep. Tensile force was applied to polymer films (5.5 mm (width) × 1.5 mm (thickness)) in oscillation mode with a temperature ramp. The amplitude of the oscillation is 0.1% in strain. The frequency of the oscillation is 1 Hz. The analysis was held in a heat−cool−heat pattern. In the first heating cycle, the experiment starts at room temperature and increases to 100 °C. Then, the films were cooled to −60 °C and heated back to 100 °C in the second heating cycle. The temperature ramp rate was 3 °C/min.

4.11.2. DMA Strain Recovery Cyclic Testing. Unconstrained strain recovery testing for 75 wt % SA was performed using a DMA 850 (TA instrument) in tension mode. Samples were printed as an ASTM Standard D638 Type IV scaled by a factor of 0.3 (~2.2 mm width, 10 mm gauge length, 1.3 mm thickness). Before testing, samples were annealed at 80 °C in an oven for 2 h. The samples were then cooled to room temperature and clamped in the DMA. Testing consisted of heating the specimen to 65 °C with a tensile force of 1 mN and a heating rate of 3 °C/min by the DMA to remove thermal history. In the stress-controlled test, films were first heated to 65 °C. After the temperature stabilized, the films were stretched to 100% strain and stabilized at 65 °C for 5 min. The temperature was then cooled to 0 °C at a rate of 3 °C/min and strain was maintained at 100%. The film was then stabilized at 0 °C for 8 min to complete crystallization in the deformed shape. Then, the film was heated back to 65 °C at a rate of 3 °C/min and a tensile force of 1 mN. The cycle of deformation, cooling, and heating with constant stress was repeated five times. The change of strain in the cycles was recorded.

4.11.3. DMA Stress Recovery. Constrained stress recovery testing for 75 wt % SA was performed using a DMA 850 (TA instrument) in tension mode. Samples were printed as an ASTM Standard D638 Type IV scaled by a factor of 0.3 (~2.2 mm width, 10 mm gauge length, 1.3 mm thickness). Before testing, samples were annealed at 80 °C in an oven for 2 h. The samples were then cooled to room temperature and clamped in the DMA. Testing consisted of heating the specimen to 65 °C with a tensile force of 1 mN and a heating rate of 3 °C/min by the DMA to remove thermal history. In the stress-controlled test, films were first heated to 65 °C. After the temperature stabilized, the films were stretched to 100% strain and stabilized at 65 °C for 5 min. The temperature was then cooled to 0 °C at a rate of 3 °C/min and strain was maintained at 100%. The film was then stabilized at 0 °C for 8 min to complete crystallization in the deformed shape. Then, the film was heated back to 65 °C at a rate of 3 °C/min with strain controlled at 100%. The corresponding stress was recorded for the study. Results are provided in Figure 5B.

4.12. Calculation of Strain Recovery (R_r) and Strain Fixity (R_f). From the DMA strain recovery cyclic testing (above), the shape recovery parameters were calculated using the stroke values of the initial length (ε_0), the deformation length after heating (ε_m), the fixation length after load removal (ε_u), and the final length after the temperature ramp during the recovery process (ε_r), as described previously in the literature.[68] Results provided in Figure 5C.

$$R_f = \left(1 - \frac{\varepsilon_m - \varepsilon_u}{\varepsilon_m}\right) \times 100 \quad (3)$$

$$R_r = \left(1 - \frac{\varepsilon_r - \varepsilon_0}{\varepsilon_0}\right) \times 100 \quad (4)$$

4.13. Digital Image Correlation (DIC). After the specimens were 3D printed into ASTM Standard D638 Type IV scaled by a factor of 0.3 (~2.2 mm width, 10 mm gauge length, 1.3 mm thickness), they were painted with a layer of white silicone spray paint. After drying for ~15 min in air, speckles of black silicone spray paint were applied to the specimens. The samples were stretched at 200%/min on a tensile tester (Instron 34TM5 with a 100 Newton load cell) until failure. Images were captured of the specimen approximately every second using a Baumer VCXU32M (resolution of 2048 × 1536 pixels). A custom DIC (digital image correlation) software (https://github.com/AnthonyA28/AA-DIC-) was used to analyze the images. An area of interest (from pixel (1,342,780) to pixel (1,672,830)) within the specimen was chosen and a grid of points 15 pixels apart within the area of interest was formed. For each point, a window of 30 × 30 pixels, with the point being in the center, was formed. The window (and thus the point) was tracked and updated on each consecutive image. The engineering strain was determined by the gradient at each point. Due to the horizontal symmetry of the sample, the strains were averaged along the y direction. To prevent blending the distinct border between the hard and soft domains, no smoothing was performed along the x direction. The strain in the soft segments was determined by averaging 6 horizontally averaged points, rows of points 8−13. The bulk strain was computed by the displacement between the clamps. The multimaterial (75/65/75) SA wt % can be modeled as three materials in series. In that case, each segment would bear the same stress, the same as the bulk stress: $\sigma_{stiff,1} = \sigma_{soft} = \sigma_{stiff,2} = \sigma_{bulk}$. The maximum stress experienced by the multilateral before failure was under 2.3 MPa for all trials. The stress can be matched to those experienced on tensile tests on the single material equivalents. At 2.3 MPa, the pure 75 wt % SA samples undergo a strain of 6.4% (range of 2.8% std dev 1.3%). The local strain within the stiff domains of the multimaterial just before failure, (when $\sigma_{stiff,1} = \sigma_{stiff,2} \sim 2.3$ MPa) computed by DIC, was 4.0% (range of 1.9% std of 0.92%). The model prediction of 6.4% is reasonably close to the strain computed experimentally by DIC of 4.0%. Results provided in Figure 6C.

4.14. Thermal Control for Shape-Memory Videos. A custom-built environmental chamber capable of temperature and humidity control was used to record shape change during a temperature ramp and ambient humidity. The chamber was coupled with a thermocouple capable of providing real-time temperature readings of the atmosphere. Samples were adhered to microscope slides and a ramp rate of ~2 °C/min was used.

4.15. Scanning Electron Microscopy (SEM). SEM was performed using an FEI Quanta 650 SEM, which features three imaging modes: high vacuum, low vacuum, and environmental SEM (ESEM), and can resolve features down to ~5 nm. SEM was used under high vacuum to image the surface of the 3D-printed Kelvin foam. For improved imaging, the sample was sputtered with Au using an EMS sputter coater (Electron Microscopy Science). Sputtering was conducted for 1.75 min at 40 mA.

■ ASSOCIATED CONTENT

Supporting Information

The Supporting Information is available free of charge at https://pubs.acs.org/doi/10.1021/acsami.3c07172.

Materials and methods; thermomechanical characterization, and 3D printing (PDF)

Compression and recovery of a Kelvin foam truss comprising 75 wt % SA. The sample was melted using a heat gun before applying compression to 75% strain. The sample was then left compressed for ~5 min before removing the load, followed by heating the sample again using an external heat gun to recover the original lattice structure (MP4)

https://doi.org/10.1021/acsami.3c07172
ACS Appl. Mater. Interfaces 2023, 15, 34097−34107

A 3D-printed multimaterial bar comprising regions of 90, 75, and 60 wt % SA from top to bottom. The bar starts in a twisted temporary shape and upon heating in a custom-built temperature-controlled environmental chamber, it unwinds to the permanent (original as-printed) shape showing multistage shape memory (MP4)

A 3D-printed multimaterial butterfly starting in a "frozen" temporary shape with the wings up, followed by heating in a custom-built temperature-controlled environmental chamber, leading to relaxation of the wings (MP4)

AUTHOR INFORMATION

Corresponding Author

Zachariah A. Page − *Department of Chemistry, The University of Texas at Austin, Austin, Texas 78712, United States;* orcid.org/0000-0002-1013-5422; Email: zpage@utexas.edu

Authors

Adrian K. Rylski − *Department of Chemistry, The University of Texas at Austin, Austin, Texas 78712, United States*

Tejas Maraliga − *McKetta Department of Chemical Engineering, The University of Texas at Austin, Austin, Texas 78712, United States*

Yudian Wu − *Department of Chemistry, The University of Texas at Austin, Austin, Texas 78712, United States*

Elizabeth A. Recker − *McKetta Department of Chemical Engineering, The University of Texas at Austin, Austin, Texas 78712, United States*

Anthony J. Arrowood − *McKetta Department of Chemical Engineering, The University of Texas at Austin, Austin, Texas 78712, United States*

Gabriel E. Sanoja − *McKetta Department of Chemical Engineering, The University of Texas at Austin, Austin, Texas 78712, United States;* orcid.org/0000-0001-5477-2346

Complete contact information is available at: https://pubs.acs.org/10.1021/acsami.3c07172

Author Contributions

Conceptualization: A.K.R. and Z.A.P.; methodology: A.K.R., T.M., Y.W., E.A.R., A.J.A., G.E.S., and Z.A.P.; investigation: A.K.R., T.M., Y.W., E.A.R., and A.J.A.; visualization: A.K.R., Y.W., E.A.R., A.J.A., and Z.A.P.; funding acquisition: Z.A.P. and G.E.S.; project administration: Z.A.P.; supervision: Z.A.P. and G.E.S.; writing—original draft: A.K.R. and Z.A.P.; and writing—review & editing: A.K.R., T.M., Y.W., E.A.R., A.J.A., G.E.S., and Z.A.P.

Notes

The authors declare no competing financial interest.

ACKNOWLEDGMENTS

The authors acknowledge primary support by the National Science Foundation under Grant No. DMR-2045336 (A.K.R., T.M., E.A.R., Z.A.P.; material synthesis and characterization, 3D printing, supervision, and writing). Partial support was provided by the National Science Foundation under Grant No. AM-2110526 (Y.W., Z.A.P.; dynamic mechanical analysis and photorheology), the Cockrell School of Engineering (A.J.A., G.E.S.; digital image correlation), and the Robert A. Welch Foundation under Grant No. F-2007 (Z.A.P.; partial materials and supplies support). The authors additionally thank Keldy S. Mason for SEM assistance and Zhanrui Zhang for environmental chamber assistance.

ABBREVIATIONS

DLP, digital light processing
T_g, glass-transition temperature
T_m, melting temperature
ΔH_m, enthalpy change of melting
E, tensile modulus
SA, stearyl acrylate
LA, lauryl acrylate
BAPO, bisacylphosphine oxide
TPGDA, tripropylene glycol diacrylate
RT-FTIR, real-time Fourier transform infrared spectroscopy
ITO, indium tin oxide
DSC, differential scanning calorimetry
χ_c, degree of crystallinity
TGA, thermogravimetric analysis
T_{d5}, 5% weight-loss temperature
ε_f, strain at fracture
ε_0, initial strain
ε_m, max strain
ε_u, strain after unloading
ε_r, strain after recovery
SEM, scanning electron microscopy

REFERENCES

(1) Narupai, B.; Nelson, A. 100th Anniversary of Macromolecular Science Viewpoint: Macromolecular Materials for Additive Manufacturing. *ACS Macro Lett.* **2020**, *9*, 627−638.

(2) Demoly, F.; André, J.-C. Roadmapping 4D Printing through Disruptive Ideas. In *Smart Materials in Additive Manufacturing, Volume 1 : 4D Printing Principles and Fabrication*; Elsevier, 2022; pp 419−455.

(3) Rafiee, M.; Granier, F.; Tao, R.; Bhérer-Constant, A.; Chenier, G.; Therriault, D. Multi-Material, Multi-Process, Planar, and Non-planar Additive Manufacturing of Piezoelectric Devices. *Adv. Eng. Mater.* **2022**, *24*, No. 2200294.

(4) Akbar, I.; El Hadrouz, M.; El Mansori, M.; Lagoudas, D. Toward Enabling Manufacturing Paradigm of 4D Printing of Shape Memory Materials: Open Literature Review. *Eur. Polym. J.* **2022**, *168*, No. 111106.

(5) Fu, P.; Li, H.; Gong, J.; Fan, Z.; Smith, A. T.; Shen, K.; Khalfalla, T. O.; Huang, H.; Qian, X.; McCutcheon, J. R.; Sun, L. 4D Printing of Polymers: Techniques, Materials, and Prospects. *Prog. Polym. Sci.* **2022**, *126*, No. 101506.

(6) Mahmoud, D. B.; Schulz-Siegmund, M. Utilizing 4D Printing to Design Smart Gastroretentive, Esophageal, and Intravesical Drug Delivery Systems. *Adv. Healthcare Mater.* **2023**, *12*, No. 2202631.

(7) Chi, Y.; Li, Y.; Zhao, Y.; Hong, Y.; Tang, Y.; Yin, J. Bistable and Multistable Actuators for Soft Robots: Structures, Materials, and Functionalities. *Adv. Mater.* **2022**, *34*, No. 2110384.

(8) Kouka, M. A.; Abbassi, F.; Habibi, M.; Chabert, F.; Zghal, A.; Garnier, C. 4D Printing of Shape Memory Polymers, Blends, and Composites and Their Advanced Applications: A Comprehensive Literature Review. *Adv. Eng. Mater.* **2023**, *25*, No. 2200650.

(9) Wu, X.; Huang, W. M.; Zhao, Y.; Ding, Z.; Tang, C.; Zhang, J. Mechanisms of the Shape Memory Effect in Polymeric Materials. *Polymers* **2013**, *5*, 1169−1202.

(10) Wu, J.; Zhao, Z.; Kuang, X.; Hamel, C. M.; Fang, D.; Qi, H. J. Reversible Shape Change Structures by Grayscale Pattern 4D Printing. *Multifunct. Mater.* **2018**, *1*, No. 015002.

(11) Cui, C.; An, L.; Zhang, Z.; Ji, M.; Chen, K.; Yang, Y.; Su, Q.; Wang, F.; Cheng, Y.; Zhang, Y. Reconfigurable 4D Printing of Reprocessable and Mechanically Strong Polythiourethane Covalent Adaptable Networks. *Adv. Funct. Mater.* **2022**, *32*, No. 2203720.

(12) Ge, Q.; Sakhaei, A. H.; Lee, H.; Dunn, C. K.; Fang, N. X.; Dunn, M. L. Multimaterial 4D Printing with Tailorable Shape Memory Polymers. *Sci. Rep.* **2016**, *6*, No. 31110.
(13) Fang, Z.; Song, H.; Zhang, Y.; Jin, B.; Wu, J.; Zhao, Q.; Xie, T. Modular 4D Printing via Interfacial Welding of Digital Light-Controllable Dynamic Covalent Polymer Networks. *Matter* **2020**, *2*, 1187−1197.
(14) Miao, J. T.; Ge, M.; Peng, S.; Zhong, J.; Li, Y.; Weng, Z.; Wu, L.; Zheng, L. Dynamic Imine Bond-Based Shape Memory Polymers with Permanent Shape Reconfigurability for 4D Printing. *ACS Appl. Mater. Interfaces* **2019**, *11*, 40642−40651.
(15) Podgórski, M.; Huang, S.; Bowman, C. N. Additive Manufacture of Dynamic Thiol-Ene Networks Incorporating Anhydride-Derived Reversible Thioester Links. *ACS Appl. Mater. Interfaces* **2021**, *13*, 12789−12796.
(16) Zhu, G.; Hou, Y.; Xiang, J.; Xu, J.; Zhao, N. Digital Light Processing 3D Printing of Healable and Recyclable Polymers with Tailorable Mechanical Properties. *ACS Appl. Mater. Interfaces* **2021**, *13*, 34954−34961.
(17) Fang, Z.; Shi, Y.; Mu, H.; Lu, R.; Wu, J.; Xie, T. 3D Printing of Dynamic Covalent Polymer Network with On-Demand Geometric and Mechanical Reprogrammability. *Nat. Commun.* **2023**, *14*, No. 1313.
(18) Lendlein, A.; Gould, O. E. C. Reprogrammable Recovery and Actuation Behaviour of Shape-Memory Polymers. *Nat. Rev. Mater.* **2019**, *4*, 116−133.
(19) Hu, J.; Zhu, Y.; Huang, H.; Lu, J. Recent Advances in Shape-Memory Polymers: Structure, Mechanism, Functionality, Modeling and Applications. *Prog. Polym. Sci.* **2012**, *37*, 1720−1763.
(20) Gao, M.; Meng, Y.; Shen, C.; Pei, Q. Stiffness Variable Polymers Comprising Phase-Changing Side-Chains: Material Syntheses and Application Explorations. *Adv. Mater.* **2022**, *34*, No. 2109798.
(21) Kagami, Y.; Gong, J. P.; Osada, Y. Shape Memory Behaviors of Crosslinked Copolymers Containing Stearyl Acrylate. *Macromol. Rapid Commun.* **1996**, *17*, 539−543.
(22) Anthamatten, M.; Roddecha, S.; Li, J. Energy Storage Capacity of Shape-Memory Polymers. *Macromolecules* **2013**, *46*, 4230−4234.
(23) Kuenstler, A. S.; Clark, K. D.; Read de Alaniz, J.; Hayward, R. C. Reversible Actuation via Photoisomerization-Induced Melting of a Semicrystalline Poly(Azobenzene). *ACS Macro Lett.* **2020**, *9*, 902−909.
(24) Chen, G.; Jin, B.; Shi, Y.; Zhao, Q.; Shen, Y.; Xie, T. Rapidly and Repeatedly Reprogrammable Liquid Crystalline Elastomer via a Shape Memory Mechanism. *Adv. Mater.* **2022**, *34*, No. 2201679.
(25) Ula, S. W.; Traugutt, N. A.; Volpe, R. H.; Patel, R. R.; Yu, K.; Yakacki, C. M. Liquid Crystal Elastomers: An Introduction and Review of Emerging Technologies. *Liq. Cryst. Rev.* **2018**, *6*, 78−107.
(26) Shiblee, M. N. I.; Ahmed, K.; Khosla, A.; Kawakami, M.; Furukawa, H. 3D Printing of Shape Memory Hydrogels with Tunable Mechanical Properties. *Soft Matter* **2018**, *14*, 7809−7817.
(27) Zhang, B.; Zhang, W.; Zhang, Z.; Zhang, Y.-F.; Hingorani, H.; Liu, Z.; Liu, J.; Ge, Q. Self-Healing Four-Dimensional Printing with an Ultraviolet Curable Double-Network Shape Memory Polymer System. *ACS Appl. Mater. Interfaces* **2019**, *11*, 10328−10336.
(28) Xu, Z.-Y.; Li, L.; Shi, L.; Yang, K.; Wang, Y. Effect of Self-Nucleation and Stress-Induced Crystallization on the Tunable Two-Way Shape-Memory Effect of a Semicrystalline Network. *Macromolecules* **2022**, *55*, 5104−5114.
(29) Shiblee, M. N. I.; Ahmed, K.; Kawakami, M.; Furukawa, H. 4D Printing of Shape-Memory Hydrogels for Soft-Robotic Functions. *Adv. Mater. Technol.* **2019**, *4*, No. 1900071.
(30) Thijssen, Q.; Quaak, A.; Toombs, J.; De Vlieghere, E.; Parmentier, L.; Taylor, H.; Van Vlierberghe, S. Volumetric Printing of Thiol-Ene Photo-Cross-Linkable Poly(ε -caprolactone): A Tunable Material Platform Serving Biomedical Applications. *Adv. Mater.* **2023**, *35*, No. 2210136.
(31) Kuenstler, A. S.; Hernandez, J. J.; Trujillo-Lemon, M.; Osterbaan, A.; Bowman, C. N. Vat Photopolymerization Additive Manufacturing of Tough, Fully Recyclable Thermosets. *ACS Appl. Mater. Interfaces* **2023**, *15*, 11111−11121.
(32) Rafiee, M.; Farahani, R. D.; Therriault, D. Multi-Material 3D and 4D Printing: A Survey. *Adv. Sci.* **2020**, *7*, No. 1902307.
(33) Sampson, K. L.; Deore, B.; Go, A.; Nayak, M. A.; Orth, A.; Gallerneault, M.; Malenfant, P. R. L.; Paquet, C. Multimaterial Vat Polymerization Additive Manufacturing. *ACS Appl. Polym. Mater.* **2021**, *3*, 4304−4324.
(34) Han, D.; Lee, H. Recent Advances in Multi-Material Additive Manufacturing: Methods and Applications. *Curr. Opin. Chem. Eng.* **2020**, *28*, 158−166.
(35) Someya, T.; Bao, Z.; Malliaras, G. G. The Rise of Plastic Bioelectronics. *Nature* **2016**, *540*, 379−385.
(36) Yuk, H.; Lu, B.; Zhao, X. Hydrogel Bioelectronics. *Chem. Soc. Rev.* **2019**, *48*, 1642−1667.
(37) Zhou, L. Y.; Fu, J.; He, Y. A Review of 3D Printing Technologies for Soft Polymer Materials. *Adv. Funct. Mater.* **2020**, *30*, No. 2000187.
(38) Zhang, Q.; Shi, Y.; Zhao, Z. A Brief Review of Mechanical Designs for Additive Manufactured Soft Materials *Soft Sci.* 2022, *2*, 2 DOI: 10.20517/ss.2021.22.
(39) Lu, P.; Ahn, D.; Yunis, R.; Delafresnaye, L.; Corrigan, N.; Boyer, C.; Barner-Kowollik, C.; Page, Z. A. Wavelength-Selective Light-Matter Interactions in Polymer Science. *Matter* **2021**, *4*, 2172−2229.
(40) Zorzetto, L.; Andena, L.; Briatico-Vangosa, F.; De Noni, L.; Thomassin, J. M.; Jérôme, C.; Grossman, Q.; Mertens, A.; Weinkamer, R.; Rink, M.; Ruffoni, D. Properties and Role of Interfaces in Multimaterial 3D Printed Composites. *Sci. Rep.* **2020**, *10*, No. 22285.
(41) Zhong, M.; Wang, R.; Kawamoto, K.; Olsen, B. D.; Johnson, J. A. Quantifying the Impact of Molecular Defects on Polymer Network Elasticity. *Science* **2016**, *353*, 1264−1268.
(42) Keith, A. N.; Vatankhah-Varnosfaderani, M.; Clair, C.; Fahimipour, F.; Dashtimoghadam, E.; Lallam, A.; Sztucki, M.; Ivanov, D. A.; Liang, H.; Dobrynin, A. V.; Sheiko, S. S. Bottlebrush Bridge between Soft Gels and Firm Tissues. *ACS Cent. Sci.* **2020**, *6*, 413−419.
(43) Cazin, I.; Gleirscher, M. O.; Fleisch, M.; Berer, M.; Sangermano, M.; Schlögl, S. Spatially Controlling the Mechanical Properties of 3D Printed Objects by Dual-Wavelength Vat Photopolymerization. *Addit. Manuf.* **2022**, *57*, No. 102977.
(44) Schwartz, J. J.; Boydston, A. J. Multimaterial Actinic Spatial Control 3D and 4D Printing. *Nat. Commun.* **2019**, *10*, No. 791.
(45) Dolinski, N. D.; Page, Z. A.; Callaway, E. B.; Eisenreich, F.; Garcia, R. V.; Chavez, R.; Bothman, D. P.; Hecht, S.; Zok, F. W.; Hawker, C. J. Solution Mask Liquid Lithography (SMaLL) for One-Step, Multimaterial 3D Printing. *Adv. Mater.* **2018**, *30*, No. 1800364.
(46) Zhang, X.; Xi, W.; Huang, S.; Long, K.; Bowman, C. N. Wavelength-Selective Sequential Polymer Network Formation Controlled with a Two-Color Responsive Initiation System. *Macromolecules* **2017**, *50*, 5652−5660.
(47) Kuang, X.; Wu, J.; Chen, K.; Zhao, Z.; Ding, Z.; Hu, F.; Fang, D.; Qi, H. J. Grayscale Digital Light Processing 3D Printing for Highly Functionally Graded Materials. *Sci. Adv.* **2019**, *5*, No. eaav579.
(48) Rossegger, E.; Strasser, J.; Höller, R.; Fleisch, M.; Berer, M.; Schlögl, S. Wavelength Selective Multi-Material 3D Printing of Soft Active Devices Using Orthogonal Photoreactions. *Macromol. Rapid Commun.* **2022**, *44*, No. 2200586.
(49) Rylski, A. K.; Cater, H. L.; Mason, K. S.; Allen, M. J.; Arrowood, A. J.; Freeman, B. D.; Sanoja, G. E.; Page, Z. A. Polymeric Multimaterials by Photochemical Patterning of Crystallinity. *Science* **2022**, *378*, 211−215.
(50) Creton, C. Pressure-Sensitive Adhesives: An Introductory Course. *MRS Bull.* **2003**, *28*, 434−439.
(51) Daniel, W. F. M.; Burdyńska, J.; Vatankhah-Varnoosfaderani, M.; Matyjaszewski, K.; Paturej, J.; Rubinstein, M.; Dobrynin, A. V.; Sheiko, S. S. Solvent-Free, Supersoft and Superelastic Bottlebrush Melts and Networks. *Nat. Mater.* **2016**, *15*, 183−189.

(52) Choi, C.; Okayama, Y.; Morris, P. T.; Robinson, L. L.; Gerst, M.; Speros, J. C.; Hawker, C. J.; de Alaniz, J. R.; Bates, C. M. Digital Light Processing of Dynamic Bottlebrush Materials. *Adv. Funct. Mater.* **2022**, *32*, No. 2200883.
(53) Broer, D. J.; Mol, G. N.; Challa, G. Temperature Effects on the Kinetics of Photoinitiated Polymerization of Dimethacrylates. *Polymer* **1991**, *32*, 690−695.
(54) Winter, H. H.; Chambon, F. Analysis of Linear Viscoelasticity of a Crosslinking Polymer at the Gel Point. *J. Rheol.* **1986**, *30*, 367−382.
(55) Jordan, E. F.; Feldeisen, D. W.; Wrigley, A. N. Side-Chain Crystallinity. I. Heats of Fusion and Melting Transitions on Selected Homopolymers Having Long Side Chains. *J. Polym. Sci., Part A-1: Polym. Chem.* **1971**, *9*, 1835−1851.
(56) Hong, K.; Rastogi, A.; Strobl, G. A Model Treating Tensile Deformation of Semicrystalline Polymers: Quasi-Static Stress-Strain Relationship and Viscous Stress Determined for a Sample of Polyethylene. *Macromolecules* **2004**, *37*, 10165−10173.
(57) Cooper, C. B.; Nikzad, S.; Yan, H.; Ochiai, Y.; Lai, J. C.; Yu, Z.; Chen, G.; Kang, J.; Bao, Z. High Energy Density Shape Memory Polymers Using Strain-Induced Supramolecular Nanostructures. *ACS Cent. Sci.* **2021**, *7*, 1657−1667.
(58) Fan, J.; Li, G. High Enthalpy Storage Thermoset Network with Giant Stress and Energy Output in Rubbery State. *Nat. Commun.* **2018**, *9*, No. 642.
(59) Meng, Y.; Jiang, J.; Anthamatten, M. Body Temperature Triggered Shape-Memory Polymers with High Elastic Energy Storage Capacity. *J. Polym. Sci., Part B: Polym. Phys.* **2016**, *54*, 1397−1404.
(60) Lin, T.; Tang, Z.; Guo, B. New Design Strategy for Reversible Plasticity Shape Memory Polymers with Deformable Glassy Aggregates. *ACS Appl. Mater. Interfaces* **2014**, *6*, 21060−21068.
(61) Fulati, A.; Uto, K.; Ebara, M. Influences of Crystallinity and Crosslinking Density on the Shape Recovery Force in Poly(ε-Caprolactone)-Based Shape-Memory Polymer Blends. *Polymers* **2022**, *14*, No. 4740.
(62) Fang, Z.; Zheng, N.; Zhao, Q.; Xie, T. Healable, Reconfigurable, Reprocessable Thermoset Shape Memory Polymer with Highly Tunable Topological Rearrangement Kinetics. *ACS Appl. Mater. Interfaces* **2017**, *9*, 22077−22082.
(63) Santiago, D.; Fabregat-Sanjuan, A.; Ferrando, F.; De La Flor, S. Recovery Stress and Work Output in Hyperbranched Poly-(Ethyleneimine)-Modified Shape-Memory Epoxy Polymers. *J. Polym. Sci., Part B: Polym. Phys.* **2016**, *54*, 1002−1013.
(64) Lakhera, N.; Yakacki, C. M.; Nguyen, T. D.; Frick, C. P. Partially Constrained Recovery of (Meth)Acrylate Shape-Memory Polymer Networks. *J. Appl. Polym. Sci.* **2012**, *126*, 72−82.
(65) Peixoto, C.; Zille, A.; da Silva, F. A.; Carneiro, O. S. Shape Memory Polymers as Actuators: Characterization of the Relevant Parameters under Constrained Recovery. *Polym. Eng. Sci.* **2021**, *61*, 2522−2535.
(66) Peng, B.; Yang, Y.; Cavicchi, K. A. Sequential Shapeshifting 4D Printing: Programming the Pathway of Multi-Shape Transformation by 3D Printing Stimuli-Responsive Polymers. *Multifunct. Mater.* **2020**, *3*, No. 042002.
(67) Hong, K.; Rastogi, A.; Strobl, G. A Model Treating Tensile Deformation of Semicrystalline Polymers: Quasi-Static Stress-Strain Relationship and Viscous Stress Determined for a Sample of Polyethylene. *Macromolecules* **2004**, *37*, 10165−10173.
(68) Liu, W.; He, Y.; Leng, J. Shape Memory Supramolecular Polyurea with Adjustable Toughness and Ultrahigh Energy Density. *ACS Appl. Polym. Mater.* **2022**, *4*, 6092−6102.

https://doi.org/10.1021/acsami.3c07172
ACS Appl. Mater. Interfaces 2023, 15, 34097−34107